Switching from two-electron to four-electron photocatalytic pure water splitting via band bending engineering with boosted activity

Wenlong Fu [a,b], Xiangjiu Guan [b,c], Haochen Wu [b], Maochang Liu [b,c,*]

[a] Shaanxi International Research Center for Soft Matter, State Key Laboratory for Mechanical Behavior of Materials, School of Materials Science and Engineering, Xi'an Jiaotong University, Xi'an 710049, PR China
[b] International Research Center for Renewable Energy, State Key Laboratory of Multiphase Flow in Power Engineering, Xi'an Jiaotong University, Xi'an, Shaanxi 710049, PR China
[c] Suzhou Academy of Xi'an Jiaotong University, Suzhou, Jiangsu 215123, PR China

ARTICLE INFO

ABSTRACT

Photocatalytic pure water splitting using particulate photocatalyst is usually restricted by the extremely slow reaction kinetics. Herein, we demonstrated a novel Z-scheme heterojunction, composed of a phosphatized p-type gallium indium zinc oxynitride (GIZON-P) and a n-type g-C_3N_4 (CN). Results show that phosphorization could reduce hole concentration within p-type GIZON, resulting in the transition of Z-scheme band structure into type-II style. This transformation leads to a completely changed reaction mechanism, i.e., from a two-electron H_2/H_2O_2 production to a four-electron H_2/O_2 generation. Although this four-electron pathway is dynamically unfavorable, the rapid charge separation by the type-II band arrangement together with thin InP layer at the surface of GIZON-P could remarkably accelerate the rate-limited O_2-evolution process. The phosphatized composite presents an excellent photocatalytic performance, with a H_2/O_2 rate of 1340/643 μmol h g. The gained quantum yield of 12.6% at 430 nm is among the best results in photocatalytic pure water splitting.

1. Introduction

Photocatalytic overall water splitting is considered to be a commercially viable process for the production of renewable energy in the near future [1–5]. As the endothermic reaction, only energy input isn't less than the enthalpy change (ΔH) to realize the disintegration of water [6,7]. Basically, the process could usually be conducted via a two-electron pathway ($H_2O \rightarrow 1/2\,H_2 + 1/2\,H_2O_2$, $\Delta H = 381$ kJ/mol) or a four-electron pathway ($H_2O \rightarrow H_2 + 1/2\,O_2$, $\Delta H = 286$ kJ/mol) [8]. Thermodynamically, the four-electron process outperforms the two-electron route. However, the formation of various intermediates (such as, HO•, •O•, HOO•) during four-electron oxygen evolution severely limit the reaction kinetics of the four-electron pathway [9]. In this case, when the valence band maximum (VBM) of semiconductor is additionally positive with respect to the formation potential of H_2O_2 (1.78 V vs. SHE), water prefers to capture photogenerated holes through a two-electron path [10,11].

Despite the superiority of the two-electron pathway, the generation of H_2O_2 will, on one hand, poison the photocatalysts by corroding their surface [12,13]. On the other hand, accumulation of H_2O_2 in the reaction solution will unavoidably induce severe reverse reaction [14,15]. More importantly, as shown in the reaction formulas, more H_2 could be produced from the four-electron photocatalytic process. Consequently, direct water splitting via four-electron photocatalysis shows a workable preference from the point view of sustainable green fuel production. In principle, tailoring the position of VBM by elemental doping to an intermediate potential between O_2 and H_2O_2 evolution could manipulate the reaction from two-electron path to four-electron mechanism [16]. However, it is still the slow reaction kinetics that restrict the conversion efficiency. Therefore, it's of great value to manipulate the VBM to a suitable position and simultaneously conquer the slow reaction kinetics from rugged four-electron transportation.

Suitable heterojunction can be employed to direct the transfer of photoinduced holes, which provides an effective method for promoting the reaction kinetics [17–19]. For instance, both CoO and Co_3O_4 could combine with g-C_3N_4 nanotubes to form a respective type-II and type-I heterojunction. As a faster charge shift and stronger electronic interaction, CoO/C_3N_4 shows a better photocatalytic performance [20]. In

addition, it is found that sacrificial agent (triethanolamine) assimilated over C_3N_4 surface could uplift the Fermi level and thus achievement of the regulation of interfacial band bending. For example, when applied to a type-II heterojunction, $C_3N_4/W_{18}O_{49}$, the band alignment the composite could be switched to a direct Z-scheme mode, leading to an impressive meliorated photocatalytic performance [21]. These examples indicate the possibility of the manipulation on electron transfer properties for improved photocatalytic performance by rational design of a heterojunction with modulated transition mechanism.

Herein, we state a regulable heterojunction photocatalyst assembled from a novel gallium indium zinc oxynitride (GIZON, p-type) and a nanosheet-like g-C_3N_4 (CN, n-type). The composite could be used for photocatalytic pure water splitting with concurrent H_2 and H_2O_2 within visible radiation. It is found that the heterojunction works in a two-electron pathway through the Z-scheme mechanism. More importantly, this reaction mechanism can be altered by simple phosphorization of GIZON. The obtained GIZON-P/CN presented an improved photocatalytic activity toward water splitting, yet via a four-electron pathway with the production of H_2 and O_2. The success relies on the reduction of the concentration of majority carriers (holes) in the p-type GIZON taken by phosphorus doping, which constitute a type-II band arrangement between GIZON-P and CN. This work thus provides a robust means for the manipulation of reaction pathway toward efficient photocatalytic overall pure water splitting.

2. Experimental

2.1. Synthesis

2.1.1. Synthesis of GIZON

GIZON was synthesized via a gel-nitridation reaction reported in the previous work [22]. Briefly, a mixed solution of ethanolamine (4 mL) and acetic acid (0.1 mL) was prepared to dissolve the metal precursor, containing gallium nitrate hydrate, indium nitrate hydrate, and zinc acetate dihydrate with a molar ratio of 1: 1: 2. Subsequently, the as-obtained mixed solution was mixed into uniform milk white gel through stirring at 65 °C for 2 h and aging at 0–2 °C for one-week, respectively. The frozen precursor firstly need to remove the extra organic component via calcination at 500 °C and collect the light-yellow fluffy powder. Ultimately, yellow inorganic oxide was nitrated at 850 °C for 10 h under ammonia flow of 200 sccm. The final dark-gray product could be labeled as GIZON.

2.1.2. Synthesis of GIZON-P

GIZON-P was also reported in the previous work [23]. Briefly, as for the phosphorization process, GIZON and sodium hypophosphite (SHP) with a certain mass ratio were grinded for 10 min, which was then transferred to a corundum boat. Afterwards, the corundum boat was heated under the Ar atmosphere at 300 °C for 2 h, followed by naturally cooling down. After purificated by centrifugation with water and ethanol, the brown products dried in vacuum could be labeled as GIZON-P.

2.1.3. Synthesis g-C_3N_4

g-C_3N_4 was fabricated according to the literature [24,25]. Briefly, urea (8 g) wrapped with a crucible was directly calcined at 550 °C for 2 h in the muffle furnace. After natural cooling, the yellow powder was gathered.

2.1.4. Synthesis of GIZON/g-C_3N_4

GIZON/g-C_3N_4 nanocrystal was prepared through a plain mechanical blending shown in Fig. S1. A certain amount of g-C_3N_4 was dispersed in the methanol (25 mL) with ultrasonication for over 30 min into a uniform solution. Afterwards, GIZON power were added in the solution and stirred to dry at ambient temperature, as well as heated in vacuum at 100 °C for 1 h to gain the tight interaction. The GIZON/g-C_3N_4 was

obtained. Based on the mass ratio X of g-C_3N_4 to GIZON, samples were labeled as GIZON/CN-X (X = 0, 0.2, 0.5, 2 and 5 wt%), respectively. For GIZON-P/CN, GIZON was just taken place by the GIZON-P to combine with g-C_3N_4 with a mass ration 0.2 wt% of C_3N_4 to GIZON-P, which could be labeled as GIZON-P/CN.

2.2. Photocatalytic tests

Typically, the reactor for photocatalytic pure water splitting test was employed in a 50 mL quartz cell, covered with an aluminum foil shell. Typically, photocatalyst reaction solution contains 30 mg photocatalyst powder and 40 mL deionized water, as well as the cocatalyst of Rh (1 wt %). After the elimination of air by blowing Ar gas for 30 min, a 300 W Xe lamp (PLS-SXE300) was as the simulated solar source to illuminate the above reactor for 5 h. Meanwhile, gas production was identified by a gas chromatograph every one hour. Besides that, light dependent photocatalytic activity was evaluated through apparent quantum yield (AQY) with 430 nm band-pass filter and calculated by the following formulation:

$$AQY = 2A_H/A_P \tag{1}$$

Where A_H and A_p are the amount of photo-induced electrons for the evolvement of H_2 and incident photons, respectively.

2.3. Characterization

The crystal structure was analyzed from X-ray diffraction (XRD) patterns through a X′Pert PRO diffractometer with a scan range between 10° and 80°. The crystallite morphologic micrographs, for example transmission electron microscopy (TEM), were conducted on a FEI Tecnai F30 microscope (300 kV). The component and bond analysis was acquired by the fourier transform infrared spectrophotometer (FTIR) spectra from a Bruker Vertex 70 FTIR spectrophotometer. X-ray photoelectron spectroscopy (XPS) data derived from an AXIS Ultra DLD XPS supply details of element chemical state, whose C 1s as the reference is the binding energy of 284.8 eV. A PTI QM-4 fluorescence spectrophotometer with a laser light source of 325 nm provide the photoluminescence (PL) emission spectroscopy to study the combination and lifetime of photo-induced carriers. UV–vis absorption spectra revealed the photo adsorption feature, tested from a Hitachi U4100 UV–vis-near-IR spectrophotometer. Zeta potential was collected on a Zetasizer Nano ZS90 apparatus. The thickness of nanosheets was determined by atomic force microscopy (AFM) images from a NT-MDT Solver Next microscope. Electron paramagnetic resonance (EPR) measurements were conducted on a Bruker EMX X-band spectrometer at room temperature.

2.4. Electrochemical tests

Electrochemical tests were executed on an electrochemical station (CHI 760D) via a typical three-electrode system, including glassy carbon electrode covered with samples as the working electrode, as well as Ag/AgCl and Pt as the respective reference electrode and counter electrode. Prior to electrochemical measurements, the electrolyte (0.5 M Na_2SO_4 solution) need remove the dissolved oxygen by being purged with Ar for 30 min. Mott-Schottky plots were recorded with the voltage range from 1.2 to 2.5 V (vs. RHE) at a frequency of 1 kHz under dark conduction.

To confirm the electron transfer number during the photocatalytic reaction, a rotating ring disk electrodes (RRDE) testing system was employed under a rotating rate of 1500 rpm, as well as 5 h photocatalytic reaction suspension as the electrolyte [26–28]. The disk potential needs to prohibit the electrolysis of water oxidation. Meanwhile, the ring voltage should have the ability in the decomposition of H_2O_2 into O_2. Electron transfer number (n) was obtained from the below formulation:

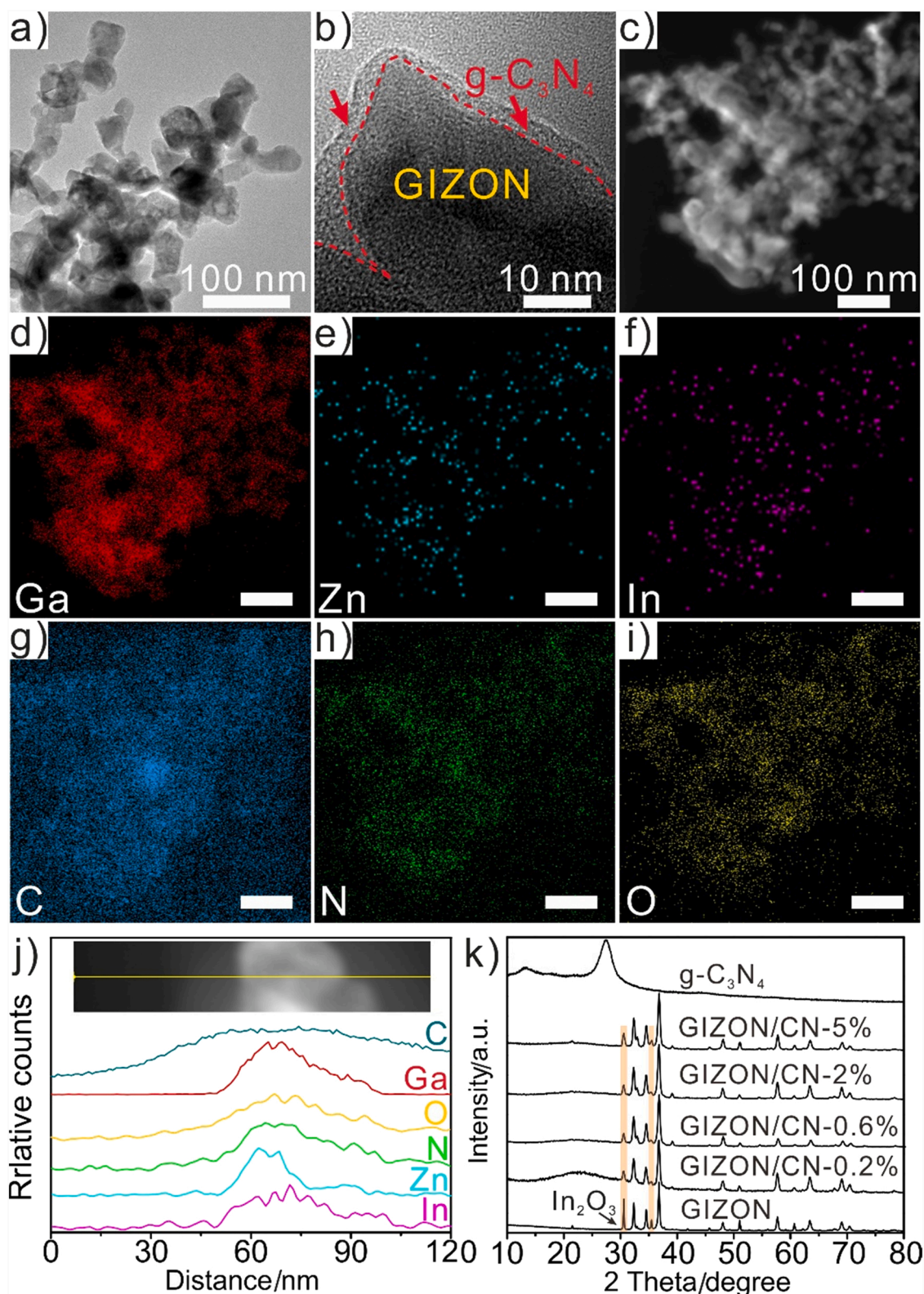$$n = 4I_{disk}/(I_{disk} + I_{ring}/N) \tag{2}$$

Fig. 1. (a) Low-magnification and (b) High-resolution TEM images of GIZON/CN 0.2% nanoparticle. (c–i) the corresponding STEM image and EDX mapping images showing the elemental distribution of GIZON/CN 0.2%. Scale bars in the images are 100 nm. (j) The EDX line scan and (k) XRD patterns of GIZON/CN.

where I_{disk} and I_{ring} are the respective current from disk and ring. N represents the RRDE collection efficiency, with an experimental value of 0.46.

2.5. Photoelectrochemical tests

The tests, such as open circuit voltage decay and transient photocurrent response, were also performed on an electrochemical station (CHI 760D) through an above mentioned three-electrode system in
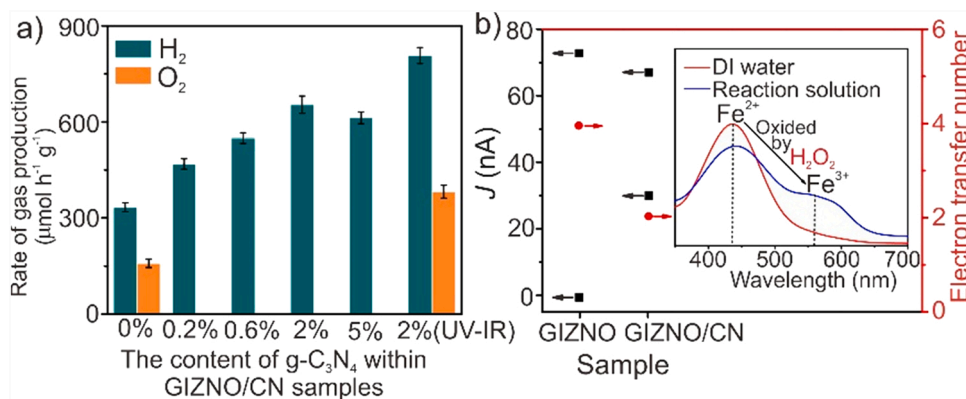
Fig. 2. Photocatalytic activity of GIZON/CN samples modified with Rh (1 wt%) as the cocatalyst. Reaction conditions: 30 mg catalyst, 40 mL H_2O; 300 W Xe lamp ($\lambda > 420$ nm or full band); (b) RRDE i-t curves under dark or light and the electron transfer number of GIZON, GIZON/CN-0.2% samples, and the inset image indicates that UV–vis absorbance spectra of H_2O_2 assay with DI water and reaction solution for GIZON/CN for overall water splitting under visible-light irradiation.

ambient conditions with light radiation. For the OCVD tests, samples need be kept with the irradiation for 300 s and then in the dark for 600 s. Based on the OCVD plots, the average carriers lifetime (τ_n) could be calculated by the equation [29,30]:

$$\tau_n = -\frac{K_B T}{q}\left(\frac{dV_{OC}}{dt}\right)^{-1} \tag{3}$$

where k_B, T and q are the Boltzmann constant, the Kelvin temperature, and the absolute value of an electron charge, respectively.

2.6. Hydrogen peroxide (H_2O_2) generation test

To verify the photocatalytic production of H_2O_2, the suspension after reaction was tested with H_2O_2 assay through UV–vis spectroscopy [27, 31,32]. The suspension was centrifuged at 8000 rpm to get rid of photocatalyst, followed added the H_2O_2 assay. After around 2 min, the mixture was characterized with the UV–vis absorption spectrum to confirm the typical peak at 560 nm, generated by H_2O_2.

3. Results and discussion

3.1. Characterization of GIZON/CN

Typically, GIZON and g-C$_3$N$_4$ were prepared by a gel-nitridation method and calcination method, respectively (see experimental details in the Supporting Information). The morphology and composition of GIZON and g-C$_3$N$_4$ were displayed in the Figs. S2 and S3. GIZON shows a core-shell structure that is the same as the one reported in our previous work [22]. g-C$_3$N$_4$ was found in the form of thin and porous nanoslices with an average thickness of about 4 nm. The synthesis procedures of compound (GIZON/CN) are illustrated in Fig. S1. Fig. 1a displays transmission electron microscopy (TEM) image of GIZON/CN. Clearly, while the original morphology of the GIZON nanoparticles was well-maintained, a strong adhesion of these nanoparticles is noticed. It should be a result of the enveloping effect taken by the two-dimension g-C$_3$N$_4$ over GIZON as demonstrated by the high-resolution TEM image (Fig. 1b). Moreover, the EDX elemental mapping images (Fig. 1, c–i) suggest existence of Ga, Zn, In, C, N, and O. Compared with Zn, slight larger distribution area of Ga, In, N, and O certifies the core-shell of GIZON nanocrystals. Moreover, the notable bigger range of C and N again reveals that GIZON nanoparticles were enveloped by g-C$_3$N$_4$. The understanding was further validated by corresponding EDX line scan (Fig. 1j). GIZON/CN composites with different weight percentage of g-C$_3$N$_4$ were then investigated from the XRD patterns (Fig. 1k). No notable diffraction peaks of CN could be observed for the composite which should be accrued from the poor crystallinity or low content of

g-C$_3$N$_4$. Nevertheless, the peak intensity of In$_2$O$_3$ was obviously decreased when GIZON was combined with g-C$_3$N$_4$. The decrement could be associated with the attraction effect of g-C$_3$N$_4$ over the surface In by weakening the In-O bonds around the surface of GIZON. What's more, the photoabsorption of GIZON/CN (Fig. S4) shows a slightly enhancement of photoabsorption around the infrared region, which might be induced by the surface defects.

To further verify the composition and chemical states, Fig. S5 also demonstrated the FTIR spectra and XPS spectra of GIZON/CN. As shown in the main characteristic FTIR signals of GIZON at 415 and 606 cm^{-1} corresponding to the respective oscillation of Zn-O and Ga-N bonds, did not change too much for all the GIZON/CN samples, while an significant decreased peak intensity at 1383 cm^{-1} representing In-O vibration was observed [33–35]. This reduction, in consistent with the XRD result, implies the weakened In-O bonds. With increment of g-C$_3$N$_4$ content, characteristic peaks of g-C$_3$N$_4$ between 1200 and 1600 cm^{-1} get stronger [36–38]. Fig. S6 shows the typical XPS spectra of the elements that are calibrated according to the C 1 s peak with the binding energy of 284.8 eV. Based on high-resolution XPS spectra of Ga (Fig. S6a), binding energy from GIZON to GIZON/CN slightly increased by 0.6 eV. It is supposed that the weakened In-O bond will automatically enhance the orbital hybridization of N and O toward Ga. No notable XPS peaks correspond to Zn 2p orbit could be observed, again certifying the surface absence of Zn (Fig. S6b). For In, it is found that the peaks representing In-N bonds were disappeared in the GIZON/CN samples, which might be a result of the encapsulation with g-C$_3$N$_4$ (Fig. S6c) [39]. The attraction from g-C$_3$N$_4$ also leads to decreased bind energies of In-O bond with the peak sets changed from 448.2/455.8 eV to 447.0/454.6 eV [40]. Moreover, with the increment of g-C$_3$N$_4$, gradual change is observed in the XPS spectra of O, N, and C peaks, also indicating the successful integration of GIZON and g-C$_3$N$_4$.

3.2. Two-electron photocatalytic pathway of GIZON-CN

The photocatalytic pure water splitting performance of GIZON/CN samples was subsequently investigated. As shown in Fig. 2a, GIZON/CN samples exhibit enhanced H$_2$ production property without any sacrificial agent relative to that of GIZON. The highest H$_2$ evolution rate reached 654 μmol h^{-1} g^{-1} over composite with a g-C$_3$N$_4$ content of 2% (designated as GIZON/CN-2%). Basically, the involvement of g-C$_3$N$_4$ could introduce lots of recombination centers within g-C$_3$N$_4$, thus impede the dissociation and migration of photo induced carriers, as demonstrated by the photoluminescence spectra (PL, Fig. S7) [41,42]. As a result, excessive amount of g-C$_3$N$_4$ in the composite resulted in decreased activity. Interestingly, different from GIZON for stoichiometric H$_2$ and O$_2$ evolution, only H$_2$ was detected under visible light irradiation. Nonetheless, taking GIZON/CN-2% as an example, when the
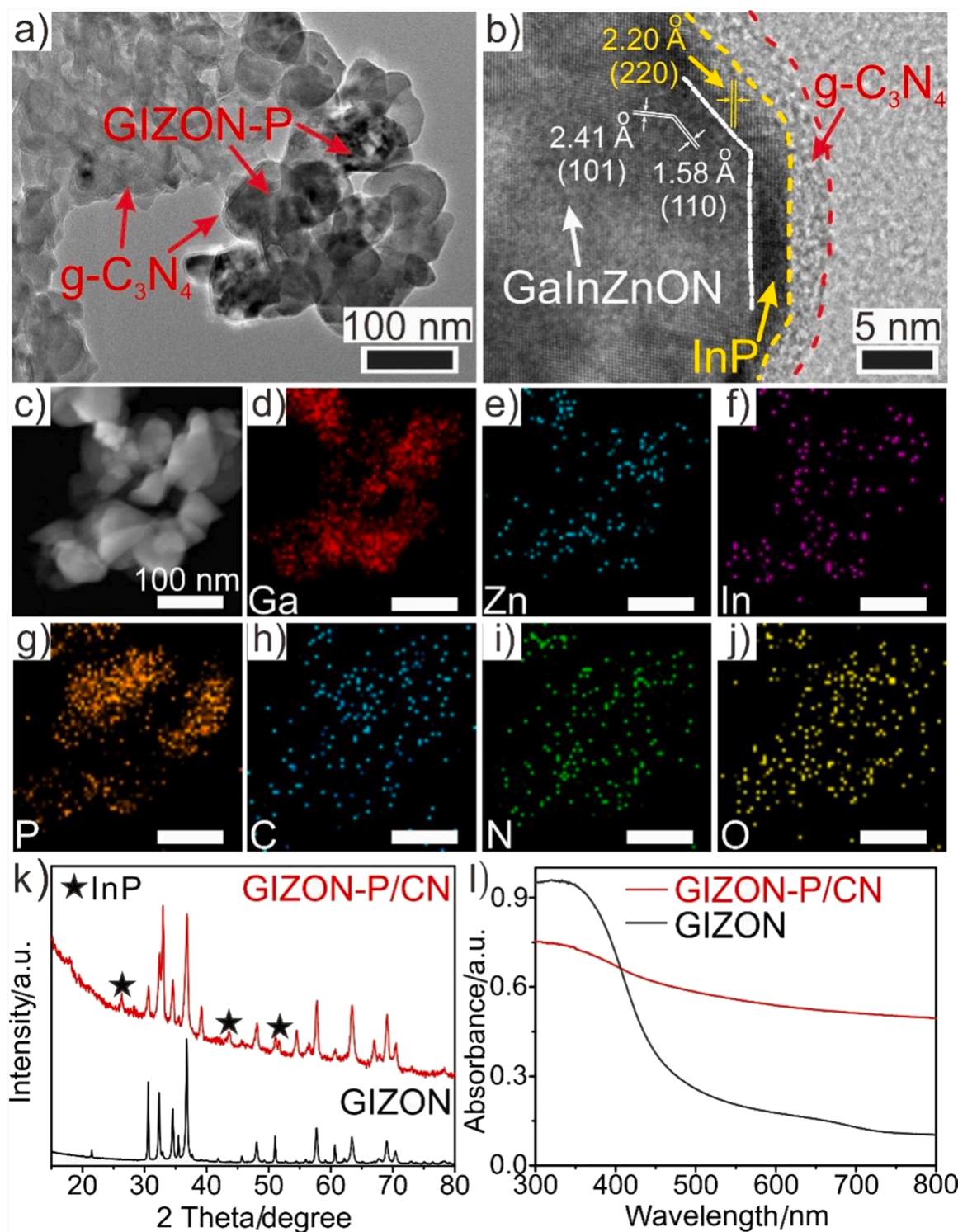
Fig. 3. (a) Low and (b) High magnification TEM images of GIZON-P/CN nanoparticles. (c–j) the corresponding EDX mapping images showing the elemental distribution in a single GIZON-P/CN nanocrystal. Scale bars in the images are 100 nm. (k) The XRD patterns and (l) UV–vis absorbance spectra of GIZON-P and GIZON-P/CN.

illumination light expands to the full-wave band, the rate of H_2 and O_2 production was simultaneously enhanced. Similar photocatalytic performance was also gained over other GIZON/CN samples (Fig. S8). To understand the behavior, we then determined the electron transfer number (N) in both GIZON and GIZON/CN under visible light illumination via the rotating ring-disk electrode (RRDE) curves (Fig. 2b). Obviously, through the combination with g-C_3N_4, the photocatalytic

process of GIZON was changed from 4e⁻ to 2e⁻ pathway, in which, the oxidation production should be H_2O_2 instead of O_2 [11,26–38,43,44]. This notion was experimentally demonstrated by a chemical titration method [30–32]. Specifically through the UV–vis spectra (inset of Fig. 2b), with the identical Fe^{3+} in DI water and the reaction solution, the absorption peak representing Fe^{2+} ion clearly decreased while a new Fe^{3+} absorption peak occurred, because of the oxidation taken by H_2O_2.
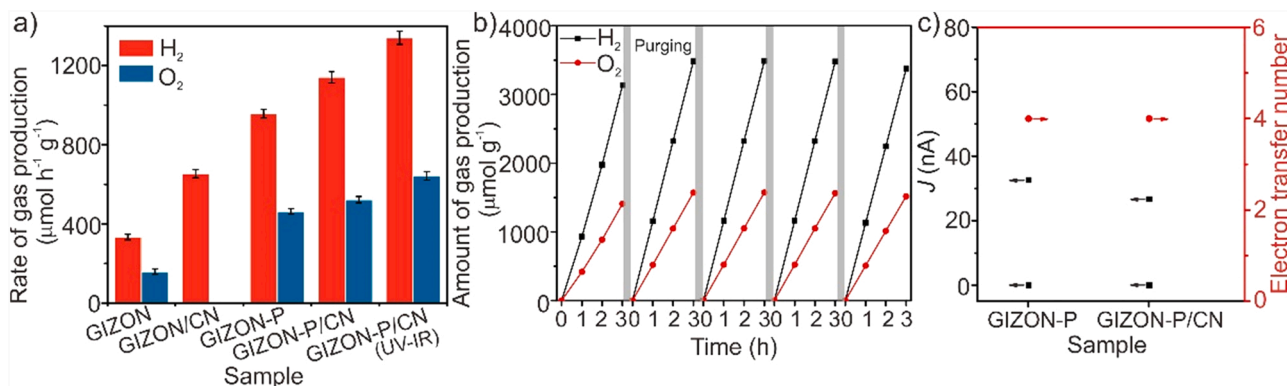
Fig. 4. (a) Photocatalytic activity of GIZON, GIZON/CN, GIZON-P and GIZON-P/CN samples modified with Rh (1 wt%) as the cocatalyst. Reaction conditions: 30 mg catalyst, 40 mL H_2O; 300 W Xe lamp ($\lambda > 420$ nm or full band). (b) Stable overall water splitting over a GIZON-P/CN sample. The reactor was purged with Ar every three hours to evacuate the gas produced. (c) RRDE i-t curves under dark or light and the electron transfer number of GIZON-P and GIZON-P/CN samples.

The production of O_2 under full-wave band irradiation should be a result of the UV-light-driven H_2O_2 decomposition. In fact, g-C_3N_4 has been reported to the selective production of H_2O_2 via a two-electron pathway due to its feeblish oxidicability, while GIZON prefers a four-electron route. This preference indicates that the oxidation sites should be on the surface of g-C_3N_4.

3.3. Characterization of GIZON-P/CN

We next tried to manipulate the photocatalytic pathway by phosphorization of the composite. In brief, phosphatized GIZON (GIZON-P) instead of GIZON was used to form a composition with g-C_3N_4 (designated as GIZON-P/CN). The morphological and structural features of GIZON-P were shown in Fig. S9. Obviously, GIZON-P also displays a heterostructure with a InP layer on the surface. For GIZON-P/CN, it is

found to be composed of GIZON-P nanoparticles and g-C_3N_4 nanosheet (Fig. 3a). Moreover, through a HRTEM image shown in Fig. 3b, a clear core-shell heterojunction between GIZON-P and g-C_3N_4 was demonstrated. The interplanar distances of 1.58 and 2.41 Å correspond to the (110) and (101) planes of the GaInZnON core. Meanwhile, the layer-to-layer spacing between the stripes is 2.20 Å, which is in consistent of (220) planes of InP. The thickness of the g-C_3N_4 layer was demonstrated to be ~4 nm as marked by the red dashed line. Fig. 3, c–j, present the mapping images of the elements involved in GIZON-P/CN. Clearly, while Ga and Zn were found in an accumulating behavior within the GIZON-P crystal, In was localized at the surface of the crystals. For C, N, and O, they distributed in accordance with the mapping area of GIZON-P/CN. P was also found to enrich at some specific sites, yet in a varied fashion compared with Ga and Zn. It is reasonable to speculate that P should be localized at the crystal surface and bonded with In, in
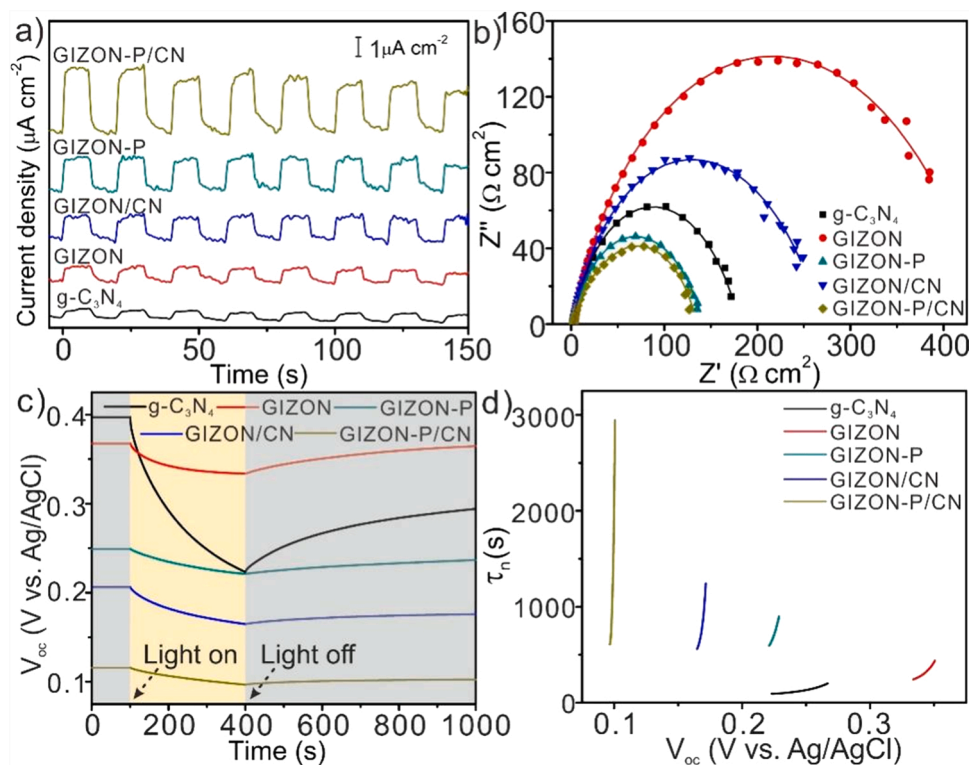

Fig. 5. (a) Transient photocurrent responses (I-t curves) of g-C_3N_4, GIZON, GIZON-P, GIZON/CN and GIZON-P/CN under the Xe lamp irradiation at a potential of 0.62 V (vs. Ag/AgCl). The light on and off periods were both for 10 s; (b) Nyquist impedance plots of samples measured at −1.1 V vs. RHE in 0.5 M Na_2SO_4 solution; (c) Open-circuit voltage decay(OCVD)curves measured for samples; (d) Electron lifetime varied with open circuit voltage calculated from the voltage decay spectra.
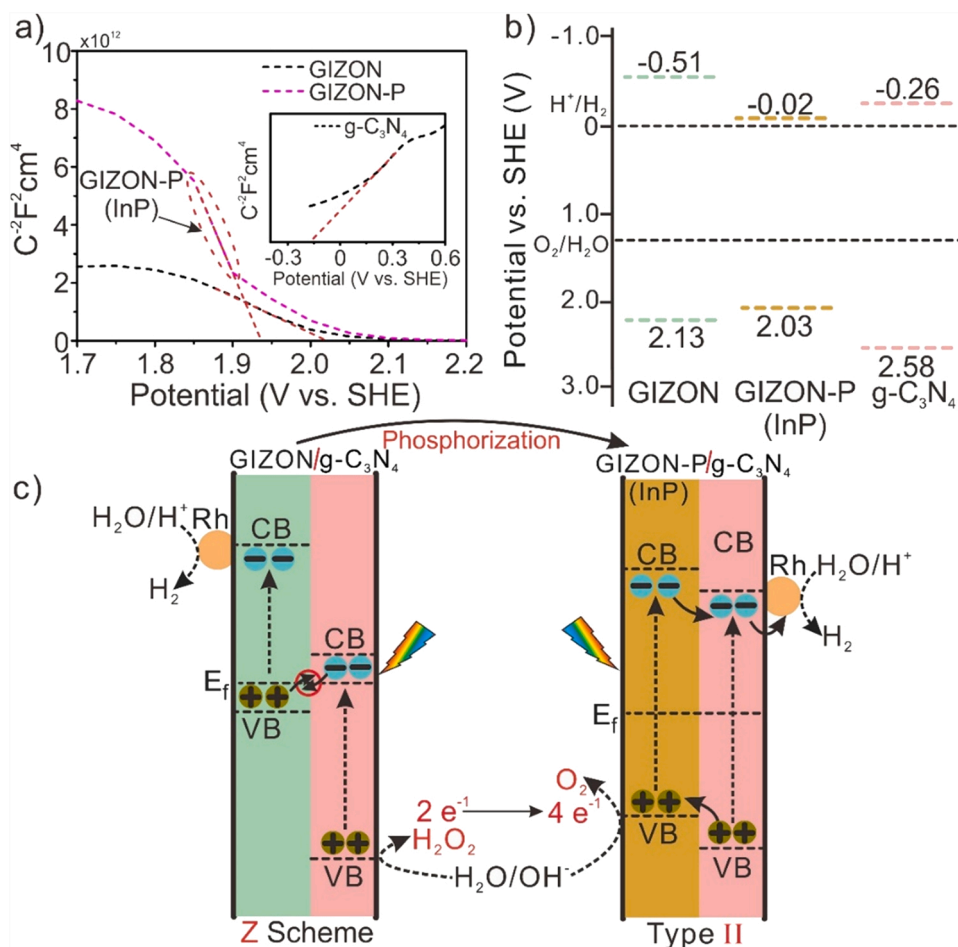
Fig. 6. (a) XPS value band spectrum and (b) Mott-schottky curve of g-C$_3$N$_4$, GIZON, and GIZON-P, respectively. Proposed mechanisms of photocatalytic activity for (c) GIZON/CN and (d) GIZON-P/CN.

agreement with aforementioned results. This surface localization led to the distinct distribution of P on the surface from that in the bulk phase, which is further confirmed from XPS spectra (24.92%) and EDS data (18.52%) as shown in Table S1. Moreover, the crystal structures and photoabsorption of GIZON and GIZON-P/CN were further investigated via the XRD pattern and UV–vis absorption spectra. Clearly, XRD peaks representing In$_2$O$_3$ in GIZON-P/CN significantly decreased, while that of InP appeared (Fig. 3k). In addition, the composite with phosphorization (GIZON-P/CN) significantly accelerated the absorbance within the visible region (Figs. 3l and S4), which was in agreement with the previous work [23].

3.4. Four-electron photocatalytic pathway of GIZON-CN

To verify the photocatalytic process, the photocatalytic performance over GIZON, GIZON-P, GIZON/CN, and GIZON-P/CN was further compared (Fig. 4a). The tests were conducted in the presence of visible light irradiation or full-wave band irradiation. It should be noticed that gas generation over GIZON-P and GIZON-P/CN under either visible light or full-wave band was a stoichiometric mixture of H$_2$ and O$_2$ close to 2:1. Particularly, GIZON-P/CN under full-wave band irradiation displayed the optimum photocatalytic performance with H$_2$ or O$_2$ evolution rates upto 1340 or 643 μmol h^{-1} g^{-1}, respectively. Meanwhile, the AQY reached 12.6% at 430 nm. As far as is known, this heterojunction presents a record-level AQY for overall water splitting, outperforming most of previously reported photocatalysts no matter in a 2e$^-$ or 4e$^-$ pathway (Table S2). The superiority could be also directly observed with the rapid bubble generation during the photocatalytic reaction (Video S1).

Besides, Fig. 4b clearly revealed the excellent stability of GIZON-P/CN. Compared with the XPS spectra of GIZON-P/CN before and after photocatalytic test in the Fig. S10, no significant difference also verified the worthy stability. We then tried to understand the reaction mechanism over the phosphatized samples. Fig. 4c also displayed the electron transfer number (N) of GIZON-P and GIZON-P/CN under the illumination of visible light via the rotating ring-disk electrode (RRDE) curves. Clearly, both GIZON-P and GIZON-P/CN showed a four-electron oxidation mechanism for the photocatalytic process. This notion suggests that phosphorization could manipulate the reaction pathway. Here, the original 2e$^-$ oxidation over GIZON/CN changed into 4e$^-$ oxygen production after phosphorization.

Supplementary material related to this article can be found online at doi:10.1016/j.apcatb.2021.121054.

3.5. Photocatalytic mechanism

To deepen the understanding of kinetics during the photocatalytic process, multiple photoelectrochemical assessments were further conducted (Fig. 5). Obviously, every photocatalyst showed expeditious and repeatable photocurrent responses with the light irradiation on/off cycles (Fig. 5a). What's more, the accelerated photocurrent intensity of GIZON-P and GIZON-P/CN reveals that phosphorization and the composition with g-C$_3$N$_4$ are crucial for enhanced photoabsorption and charge separation. Generally, phosphorization could significantly expand the light response range to arouse more carriers. Meanwhile, interfaces formed in the heterojunction promote the separation of charges. Except that, EIS Nyquist plots of g-C$_3$N$_4$, GIZON, GIZON-P,
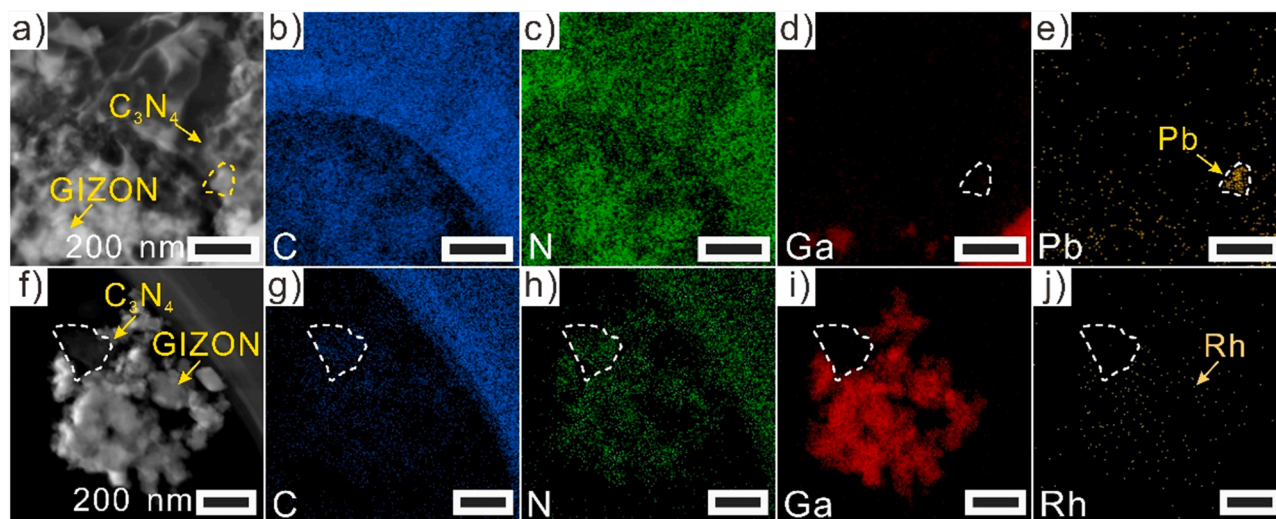
Fig. 7. STEM and EDX mapping images showing elemental distribution of GIZON/CN with the photodeposition of (a–e) PbO_2 and (f–j) Rh, respectively. Scale bars in these images are all 200 nm.

GIZON/CN and GIZON-P/CN were also delineated in the Fig. 5b. The relatively smaller arc radius of GIZON/CN and GIZON-P/CN indicates that both surface phosphorization and combination with g-C_3N_4 could lead to a lower charger transfer impedance [45]. Moreover, to investigate the electron recombination behavior, OCVD was also measured as shown in Fig. 5c. Under constant light illumination, the generation and recombination of photoinduced carriers realized the relative equilibrium under open circuit condition. Generally, open circuit potential (V_{oc}) appears to the distinction in the appearance Fermi level between samples and reference electrode [46]. As the Fermi level shift to the more negative potentials, carrier separation and electron aggregation could be enhanced around the heterojunction. The similar tendency of V_{oc} over GIZON, GIZON-P, GIZON/CN and GIZON-P/CN also verified the results gained from EIS Nyquist plots. As the dominant position of recombination, V_{oc} shows an immediate decay with the illumination terminated. Fig. 5d further depicted the electron lifetime, which was calculated through the reciprocal of decay curve normalized by V_{oc} [47]. The result also implies that surface phosphorization and the formation of heterojunction both could substantially inhibit the interfacial charge recombination.

As is well-known, photoluminescence (PL) emission originates from the radiative recombining of charge carriers (electrons and holes) in the semiconductors. Fig. S11 presented a primary PL peak around 460 nm over the total samples, which should be caused by the bandgap emission of g-C_3N_4 or GIZON. Particularly, it is found that phosphorization could remarkably reduce the PL intensities, especially at 630 nm, indicating the effectively enhanced charge separation behavior. Although all the GIZON-based composites showed much weaker peak intensity at 460 nm in comparison to of g-C_3N_4, the increased peak intensity by combination with g-C_3N_4 could not be neglected. In principle, this combination could accelerate the charge transfer between g-C_3N_4 and oxynitride, however the intrinsic recombination on g-C_3N_4 increased the PL peaks at 460 nm [19,48]. The efficient charge separation in the heterojunction composite was also certified by time-resolved fluorescence emission decay spectra (Fig. S12). Clearly, the average carriers lifetimes (τ) were determined to be 2.178, 2.824, 5.673, and 9.093 ns for GIZON, GIZON-P, GIZON/CN, and GIZON-P/CN, respectively, again demonstrating the significantly enhanced property of charge separation by surface phosphorization and heterojunction formation.

To further explore the photocatalytic pathway, the Mott-schottky curves of g-C_3N_4, GIZON, and GIZON-P were measured as shown in Fig. 6a. Obviously, together with the negative slope of Mott-schottky curves, it could be inferred that GIZON and GIZON-P are both p-type

semiconductor. Similarity, g-C_3N_4 with positive slope belongs to the n-type semiconductor. Moreover, by simulating the intersection with slope line and X axis, the flat-band potential (E_f) of g-C_3N_4, GIZON, and GIZON-P were obtained, i.e., −0.16, 2.03, 1.93 eV, respectively. The corresponding valence band maximum (E_v) and conduction band minimum (E_c) can be calculated according to the below equation,

$$E_v = E_f + m \text{ (For p type semiconductor)} \tag{4}$$

$$E_c = E_f - m \text{ (For n type semiconductor)} \tag{5}$$

where m is a constant. Here, the value of m is 0.1 [49]. Together with the energy band gaps of 2.84, 2.54, and 2.05 eV (Fig. S13), the E_v of g-C_3N_4, GIZON, and GIZON-P could be calculated to be 2.58, 2.13, 2.03 eV, respectively (Fig. 6b). Basically, to realize the equilibrium of Fermi level, the constitution of p-n junction was bound to change band level of p/n type semiconductor, so-called band uplifted effect. From the Fig. 6a, it should be noted that the absolute value of the slope for GIZON-P is higher than that of GIZON. It indicates that the concentration of majority carriers (holes) decreases after phosphorization. Spontaneously, with the XPS value band spectrum amended by the equation $E_{SHE}/V= \Phi + E_{VB}-4.44$ (E_{SHE}: potential of standard hydrogen electrode; E_{VB}: the value band measured; Φ: the electron work function of the analyzer, which is 4.46 in this work), the accurate valance band position within the heterojunction was displayed in the Fig. S14a and b [50]. Apparently, the band uplifted effect on the band level of GIZON-P/CN should be smaller than that of GIZON/CN (Fig. S14c). Therefore, proposed photocatalytic mechanisms involved in GIZON/CN and GIZON-P/CN photocatalysts could be raised as shown in Fig. 6c. For GIZON/CN, Z-scheme band alignment was built between GIZON and g-C_3N_4, namely, reduction and oxidation active sites were separated at the surface of GIZON and g-C_3N_4, respectively. As feeblish oxidizability of holes around the external of g-C_3N_4 for overall waster splitting, oxidation products were usually H_2O_2 in a $2e^-$ pathway. Through the phosphorization, the band uplifted effect on the band level decreased, leading to the transformation of Z-scheme band structure into a type-II condition. Consequently, photo-induced holes were transferred from g-C_3N_4 to GIZON-P with O_2 as the oxidation product by a direct $4e^-$ pathway. In other words, manipulation of photocatalytic pathway was realized through regulating the band uplifted effect of the p-n junction.

To experimentally verify the rationale, we also applied an in-situ method by photodeposition Rh and PbO_2 over the surface of the catalyst to demarcate the reduction/oxidation active sites, respectively. As shown in Fig. 7, for GIZON/CN, the distribution of Pb has no intersection
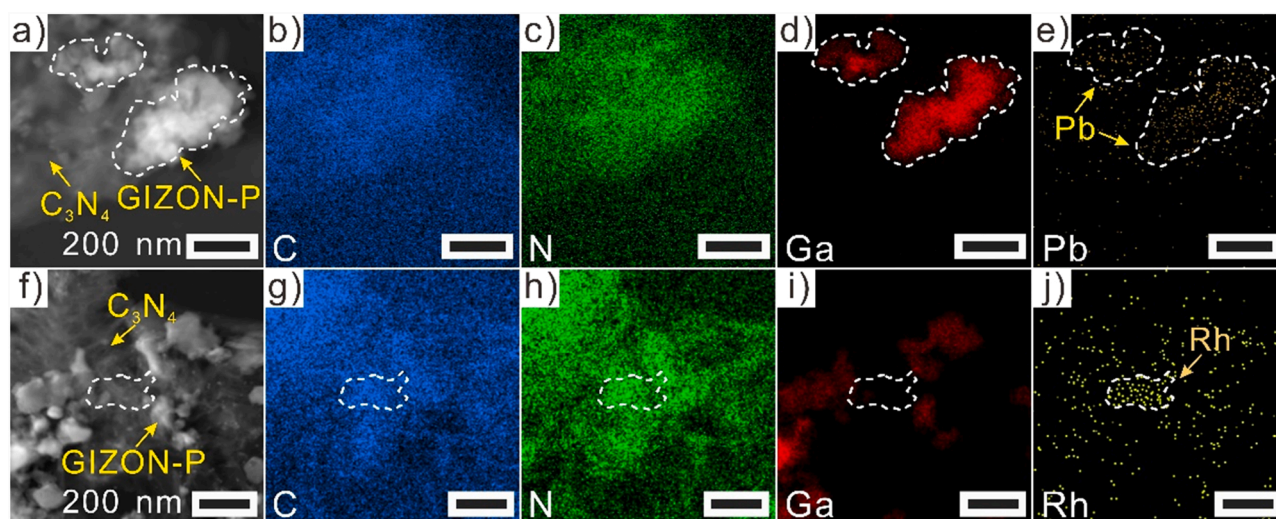
Fig. 8. STEM and EDX mapping images showing elemental distribution of GIZON-P/CN with the photodeposition of (a–e) PbO₂ and (f–j) Rh, respectively. Scale bars in these images are all 200 nm.

with that of Ga (see dashed circles in Fig. 7, a–e), but in the scope of that of C, indicating that oxidation active sites mainly exist around the surface of g-C₃N₄. Besides, most Rh nucleated on GIZON nanoparticles, however, with a notable absence at the region covered by g-C₃N₄ (see dashed cycle in Fig. 7, f–j), revealing the active reduction sites of GIZON. Similar arguments could be applied to GIZON-P/CN photocatalysts (Fig. 8). The reduction and oxidation active sites could be ascertained over the surface of g-C₃N₄ and GIZON-P, respectively.

Besides that, EPR spin-trapping experiment with DMPO as spin-trapping reagent was further carried out to verify the charge transfer mechanism over the above heterojunction. Obviously, the strong EPR signals of transient radical species (DMPO-•O₂⁻, peak intensity ratio = 1:1:1:1 and DMPO-•OH, peak intensity ratio = 1:2:2:1) were both monitored for the GIZON/CN as shown in Fig. S15a and b [51,52]. Nevertheless, there was no apparent EPR peak of DMPO-•O₂⁻ and DMPO-•OH for the GIZON-P/CN. In theory, the generation of radicals (•O₂⁻ and •OH) needs to be satisfied with the corresponding essential condition, that is the higher CB potential than the redox potential of O₂/•O₂⁻ (−0.33 V vs. SHE) or the lower VB potential than the redox potential of H₂O/•OH (1.99 V vs. SHE) [53–55]. Based on the band analysis from the Figs. 6b and S14, the band structure of heterojunction was reckoned in the Fig. S15c. For the GIZON/CN, only electrons and holes in the respective GIZON and g-C₃N₄ met the thermodynamically requirement of the formation of above radicals, which could be in consistent with the EPR spectra. In other words, holes of GIZON tended to combine with electrons of g-C₃N₄, which further validated the Z-scheme structure. For the GIZON-P/CN, no radical species detected from the EPR spectra, demonstrating a type-II band alignment between g-C₃N₄ and GIZON-P with photoinduced electrons and holes respectively allocated to the g-C₃N₄ and GIZON-P. These results both provide the direct evidence of our proposed photocatalytic mechanism (Fig. 6c).

It should be noted that after surface phosphorization, the Zeta potential value of GIZON was changed from positive to negative, the same as that of g-C₃N₄ (Fig. S16). The induced repelling effect between GIZON-P and g-C₃N₄ should promote the dispersion and uniformity of the two components during the preparation process. This notion could be also supported by the FTIR spectra of GIZON/CN and GIZON-P/CN (Fig. S17), with the observation of reduced C-N stretching vibration mode and heterocycle stretching that might be caused by the better dispersion of g-C₃N₄ [56].

4. Conclusion

In summary, we demonstrated an effective way for the manipulation of the photocatalytic pathway for pure water splitting by using particulate nanoparticles and achieve efficient activity. The success relies on phosphorization of GIZON nanoparticles for the regulation of the band uplifted effect in GIZON/CN heterojunction, through which the original Z-scheme band structure was changed into type-II band alignment. Significantly, the GIZON/CN heterojunction, which presented the H₂/H₂O₂ production from pure water splitting along a two-electron route, was changed into a direct four-electron mechanism towards overall water splitting. An excellent photocatalytic performance with respective H₂ and O₂ generation rates of 1340 and 643 μmol h⁻¹ g⁻¹ was gained over the GIZON-P/CN heterojunction photocatalyst. The corresponding AQY reached 12.6% at 430 nm, that is among the topmost published values for photocatalytic pure water splitting. We believe this effort provides an innovative strategy to achieve high photocatalytic behavior through photocatalytic pathway manipulation.

Appendix A. Supporting information

Supplementary data associated with this article can be found in the online version at doi:10.1016/j.apcatb.2021.121054.

References

[1] A. Kubacka, M. Fernandez-Garcia, G. Colon, Advanced nanoarchitectures for solar photocatalytic applications, Chem. Rev. 112 (2012) 1555–1614.

[2] Y. Tachibana, L. Vayssieres, J.R. Durrant, Artificial photosynthesis for solar water-splitting, Nat. Photonics 6 (2012) 511–518.

[3] S. Chen, T. Takata, K. Domen, Particulate photocatalysts for overall water splitting, Nat. Rev. Mater. 2 (2017) 17050.

[4] Y. Zhang, Z. Huang, J. Shi, X. Guan, C. Cheng, S. Zong, Y. Huangfu, L. Ma, L. Guo, Maleic hydrazide-based molecule doping in three-dimensional lettuce-like graphite carbon nitride towards highly efficient photocatalytic hydrogen evolution, Appl. Catal. B Environ. 272 (2020), 119009.

[5] C. Cheng, S. Zong, J. Shi, F. Xue, Y. Zhang, X. Guan, B. Zheng, J. Deng, L. Guo, Facile preparation of nanosized MoP as cocatalyst coupled with g-C$_3$N$_4$ by surface bonding state for enhanced photocatalytic hydrogen production, Appl. Catal. B Environ. 265 (2020), 118620.

[6] P. Chowdhury, G. Malekshoar, M.B. Ray, J. Zhu, A.K. Ray, Sacrificial hydrogen generation from formaldehyde with Pt/TiO$_2$ photocatalyst in solar radiation, Ind. Eng. Chem. Res. 52 (2013) 5023–5029.

[7] D. Fabian, S. Hu, N. Singh, F. Houle, T. Hisatomi, K. Domen, F. Osterloh, S. Ardo, Particle suspension reactors and materials for solar-driven water splitting, Energy Environ. Sci. 8 (2015) 2825–2850.

[8] C.J. Marzzacco, The enthalpy of decomposition of hydrogen peroxide: a general chemistry calorimetry experiment, J. Chem. Educ. 76 (1999) 1517.

[9] N.T. Suen, S.F. Hung, Q. Quan, N. Zhang, Y.J. Xu, H.M. Chen, Electrocatalysis for the oxygen evolution reaction: recent development and future perspectives, Chem. Soc. Rev. 46 (2017) 337–365.

[10] J. Liu, Y. Liu, N.Y. Liu, Y.Z. Han, X. Zhang, H. Huang, Y. Lifshitz, S.T. Lee, J. Zhang, Z.H. Kang, Metal-free efficient photocatalyst for stable visible water splitting via a two-electron pathway, Science 347 (2015) 970–974.

[11] F. Xue, Y.T. Si, M. Wang, M.C. Liu, L.J. Guo, Toward efficient photocatalytic pure water splitting for simultaneous H$_2$ and H$_2$O$_2$ production, Nano Energy 62 (2019) 823–831.

[12] A.J. Esswein, D.G. Nocera, Hydrogen production by molecular photocatalysis, Chem. Rev. 107 (2007) 4022–4047.

[13] D. Mateo, I. Esteve-Adell, J. Albero, J.F.S. Royo, A. Primo, H. Garcia, 111 oriented gold nanoplatelets on multilayer graphene as visible light photocatalyst for overall water splitting, Nat. Commun. 7 (2016), 11819-11819.

[14] X.Q. Wu, C. Zhu, L.P. Wang, S.J. Guo, Y.L. Zhang, H. Li, H. Huang, Y. Liu, J. W. Tang, Z.H. Kang, Control strategy on two-/four-electron pathway of water splitting by multidoped carbon based catalysts, ACS Catal. 7 (2017) 1637–1645.

[15] H. Wang, S.L. Jiang, W. Shao, X.D. Zhang, S.C. Chen, X.S. Sun, Q. Zhang, Y. Luo, Y. Xie, Optically switchable photocatalysis in ultrathin black phosphorus nanosheets, J. Am. Chem. Soc. 140 (2018) 3474–3480.

[16] K. Zhang, L.Y. Wang, S.W. Sheng, M. Ma, M.S. Jung, W.J. Kim, H.Y. Lee, J.H. Park, Tunable bandgap energy and promotion of H$_2$O$_2$ oxidation for overall water splitting from carbon nitride nanowire bundles, Adv. Energy Mater. 6 (2016), 1502352.

[17] G. Liu, L. Ma, L.C. Yin, G. W, H. Zhu, C. Zhen, Y.Q. Yang, Y. Liang, J. Tan, H. M. Cheng, Selective chemical epitaxial growth of TiO$_2$ islands on ferroelectric PbTiO$_3$ crystals to boost photocatalytic activity, Joule 2 (2018) 1095–1107.

[18] J. Shi, F. Chen, L. Hou, G. Li, Y. Li, X. Guan, H. Liu, L. Guo, Eosin Y bidentately bridged on UiO-66-NH$_2$ by solvothermal treatment towards enhanced visible-light-driven photocatalytic H$_2$ production, Appl. Catal. B Environ. 280 (2021), 119385.

[19] J.Q. Yan, H. Wu, H. Chen, Y.X. Zhang, F.X. Zhang, S.F. Liu, Fabrication of TiO$_2$/C$_3$N$_4$ heterostructure for enhanced photocatalytic Z-scheme overall water splitting, Appl. Catal. B Environ. 191 (2016) 130–137.

[20] Y.X. Zhu, T. Wan, X.M. Wen, D.W. Chu, Y.J. Jiang, Tunable type I and II heterojunction of CoO$_x$ nanoparticles confined in g-C$_3$N$_4$ nanotubes for photocatalytic hydrogen production, Appl. Catal. B Environ. 244 (2019) 814–822.

[21] Z.F. Huang, J.J. Song, X. Wang, L. Pan, K. Li, X.W. Zhang, L. Wang, J.J. Zou, Switching charge transfer of C$_3$N$_4$/W$_{18}$O$_{49}$ from type-II to Z-scheme by interfacial band bending for highly efficient photocatalytic hydrogen evolution, Nano Energy 40 (2017) 308–316.

[22] W.L. Fu, X.J. Guan, Z.X. Huang, M.C. Liu, L.J. Guo, Efficient photocatalytic overall water splitting over a core-shell GaInZnON@GaInON homojunction, Appl. Catal. B Environ. 255 (2019), 117741.

[23] W.L. Fu, X.J. Guan, Y.T. Si, L.J. Guo, Phosphatized GaZnInON nanocrystals with core-shell structures for efficient and stable pure water splitting via four-electron photocatalysis, Chem. Eng. J. 410 (2021), 128391.

[24] G. Zhang, Z.A. Lan, X. Wang, Surface engineering of graphitic carbon nitride polymers with cocatalysts for photocatalytic overall water splitting, Chem. Sci. 8 (2017) 5261–5274.

[25] L. Wang, Y. Zhang, L. Chen, H. Xu, Y.J. Xiong, Solar energy conversion: 2D polymers as emerging materials for photocatalytic overall water splitting, Adv. Mater. 30 (2018), 1801955.

[26] D. Qu, J. Liu, X. Miao, M. Han, H. Zhang, Z. Cui, S. Sun, Z. Kang, H. Fan, Z. Sun, Peering into water splitting mechanism of g-C$_3$N$_4$-carbon dots metal-free photocatalyst, Appl. Catal. B Environ. 227 (2018) 418–424.

[27] J. Liu, N.Y. Liu, H. Li, L.P. Wang, X.Q. Wu, H. Huang, Y. Liu, F. Bao, Y. Lifshitz, S. T. Lee, Z.H. Kang, A critical study of the generality of the two step two electron pathway for water splitting by application of a C$_3$N$_4$/MnO$_2$ photocatalyst, Nanoscale 8 (2016) 11956–11961.

[28] S. Yang, L. Zhi, K. Tang, X. Feng, J. Maier, K. Müllen, Efficient synthesis of heteroatom (N or S)-doped graphene based on ultrathin graphene oxide-porous silica sheets for oxygen reduction reactions, Adv. Funct. Mater. 22 (2012) 3634–3640.

[29] A. Zaban, M. Greenstein, J. Bisquert, Determination of the electron lifetime in nanocrystalline dye solar cells by open-circuit voltage decay measurements, Chem. Phys. Chem. 4 (2003) 859–864.

[30] D. Zhao, T. Peng, L. Lu, P. Cai, P. Jiang, Z. Bian, Effect of annealing temperature on the phothelectrochemical properties of dye-sensitized solar cells made with mesoporous TiO$_2$ nanoparticles, J. Phys. Chem. C 112 (2008) 8486–8494.

[31] F. Guo, W.L. Shi, C. Zhu, H. Li, Z.H. Kang, CoO and g-C$_3$N$_4$ complement each other for highly efficient overall water splitting under visible light, Appl. Catal. B Environ. 226 (2018) 412–420.

[32] B. Tian, B.N. Tian, B. Smith, M.C. Scott, R.N. Hua, Q. Lei, Y. Tian, Supported black phosphorus nanosheets as hydrogen-evolving photocatalyst achieving 5.4% energy conversion efficiency at 353 K, Nat. Commun. 9 (2018) 1397.

[33] S. Muthukumaran, R. Gopalakrishnan, Structural, FTIR and photoluminescence studies of Cu doped ZnO nanopowders by co-precipitation method, Opt. Mater. 34 (2012) 1946–1953.

[34] C. Yang, B.Y. Man, H.Z. Zhuang, X.Q. Wei, M. Liu, C.S. Xue, Annealing of GaN/ZnO/Si films deposited by pulsed laser deposition, Jpn. J. Appl. Phys. 46 (2007) 526–529.

[35] A. Ayeshamariam, M. Bououdina, C. Sanjeeviraja, Optical, electrical and sensing properties of In$_2$O$_3$ nanoparticles, Mater. Sci. Semicond. Process. 16 (2013) 686–695.

[36] Y.Y. Kang, Y.Q. Yang, L.C. Yin, X.D. Kang, G. Liu, H.M. Cheng, An amorphous carbon nitride photocatalyst with greatly extended visible-light-responsive range for photocatalytic hydrogen generation, Adv. Mater. 27 (2015) 4572–4577.

[37] J.H. Li, B. Shen, Z.H. Hong, B.Z. Lin, B.F. Gao, Y.L. Chen, A facile approach to synthesize novel oxygen-doped g-C$_3$N$_4$ with superior visible-light photoreactivity, Chem. Commun. 48 (2012) 12017–12019.

[38] X.J. She, J.J. Wu, J. Zhong, H. Xu, Y.C. Yang, R. Vajtai, J. Lou, Y. Liu, D.L. Du, H. M. Li, P.M. Ajayan, Oxygenated monolayer carbon nitride for excellent photocatalytic hydrogen evolution and external quantum efficiency, Nano Energy 27 (2016) 138–146.

[39] W.K. Liu, W.T. Yuen, R.A. Stradling, Preparation of InSb substratesfor molecular beam epitaxy, J. Vac. Sci. Technol. B 13 (1995) 1539–1545.

[40] M. Mapa, K. Sivaranjani, D.S. Bhange, B. Saha, P. Chakraborty, A.K. Viswanath, C. S. Gopinath, Structure, electronic structure, optical, and dehydrogenation catalytic study of (Zn$_{1-z}$In$_z$)(O$_{1-x}$N$_x$) solid solution, Chem. Mater. 22 (2010) 565–578.

[41] A. Naseri, M. Samadi, A. Pourjavadi, A.Z. Moshfegh, S. Ramakrishna, Graphitic carbon nitride (g–C$_3$N$_4$) based photocatalysts for solar hydrogen generation: recent advances and future development directions, J. Mater. Chem. 5 (2017) 23406–23433.

[42] S.W. Cao, Q. Huang, B.C. Zhu, J.G. Yu, Trace-level phosphorus and sodium co-doping of g-C$_3$N$_4$ for enhanced photocatalytic H$_2$ production, J. Power Sources 351 (2017) 151–159.

[43] M. Han, H. Wang, S. Zhao, L. Hu, H. Huang, Y. Liu, One-step synthesis of CoO/g-C$_3$N$_4$ composites by thermal decomposition for overall water splitting without sacrificial reagents, Inorg. Chem. Front. 4 (2017) 1691–1696.

[44] Z. Li, C. Kong, G. Lu, Visible photocatalytic water splitting and photocatalytic two electron oxygen formation over Cu- and Fe-doped g-C$_3$N$_4$, J. Phys. Chem. C 120 (2016) 56–63.

[45] S.X. Hua, D. Q, L. An, W.S. Jiang, Y.J. Wen, X.Y. Wang, Z.C. Sun, Highly efficient p-type Cu$_3$P/n-type g-C$_3$N$_4$ photocatalyst through Z-scheme charge transfer route, Appl. Catal. B Environ. 240 (2019) 253–261.

[46] H. Yu, S. Zhang, H. Zhao, G. Will, P. Liu, An efficient and low-cost TiO$_2$ compact layer for performance improvement of dye-sensitized solar cells, Electrochim. Acta 54 (2009) 1319–1324.

[47] J. Bisquert, A. Zaban, M. Greenstein, I.M. Sero, Determination of rate constants for charge transfer and the distribution of semiconductor and electrolyte electronic energy levels in dye-sensitized solar cells by open-circuit photovoltage decay method, J. Am. Chem. Soc. 126 (2004) 13550–13559.

[48] J.Q. Yan, G.J. Wu, N.J. Guan, L.D. Li, Nb$_2$O$_5$/TiO$_2$ heterojunctions: synthesis strategy and photocatalytic activity, Appl. Catal. B Environ. 152 (2014) 280–288.

[49] X. Li, J.G. Yu, J.X. Low, Y.P. Fang, J. Xiao, X.B. Chen, Engineering heterogeneous semiconductors for solar water splitting, J. Mater. Chem. A 3 (2015) 2485–2534.

[50] H. Yu, R. Shi, Y.X. Zhao, T. Bian, Y. Zhao, C. Zhou, G.I.N. Waterhouse, L. Wu, C. H. Tung, T.R. Zhang, Alkali-assisted synthesis of nitrogen deficient graphitic carbon nitride with tunable band structures for efficient visible-light-driven hydrogen evolution, Adv. Mater. 29 (2017), 1605148.

[51] Y. Wang, C. Zhu, G.C. Zuo, Y. Guo, W. Xiao, Y. Dai, J. Kong, X.M. Xu, Y. Zhou, A. Xie, C. Sun, Q.M. Xiao, 0D/2D Co$_3$O$_4$/TiO$_2$ Z-Scheme heterojunction for boosted photocatalytic degradation and mechanism investigation, Appl. Catal. B Environ. 278 (2020), 119298.

[52] W. Zhao, Y. Feng, H. Huang, P. Zhou, J. Li, L. Zhang, B. Dai, J.M. Xu, F.X. Zhu, N. Sheng, D.Y.C. Leung, A novel Z-scheme Ag$_3$VO$_4$/BiVO$_4$ heterojunction photocatalyst: Study on the excellent photocatalytic performance and photocatalytic mechanism, Appl. Catal. B Environ. 245 (2019) 448–458.

[53] J. Bian, Z.Q. Zhang, J.N. Feng, M. Thangamuthu, F. Yang, L. Sun, Z. Li, Y. Qu, D. Tang, Z. Lin, F.Q. Bai, J.W. Tang, L.Q. Jing, Energy platform for directed charge

transfer in the cascade Z-scheme heterojunction: CO_2 photoreduction without a cocatalyst, Angew. Chem. Int. Ed. 60 (2021) 20906–20914.

[54] C.L. Jiang, H. Wang, Y.Q. Wang, H.B. Ji, All solid-state Z-scheme $CeO_2/ZnIn_2S_4$ hybrid for the photocatalytic selective oxidation of aromatic alcohols coupled with hydrogen evolution, Appl. Catal. B Environ. 277 (2020), 119235.

[55] X.H. Wang, X.H. Wang, J.F. Huang, S.X. Li, A. Meng, Z.J. Li, Interfacial chemical bond and internal electric field modulated Z-scheme S_v-$ZnIn_2S_4/MoSe_2$ photocatalyst for efficient hydrogen evolution, Nat. Commun. 12 (2021) 4112.

[56] Y. Zhang, J. Shi, Z. Huang, X. Guan, S. Zong, C. Cheng, B. Zheng, L. Guo, Synchronous construction of CoS_2 in-situ loading and S doping for g-C_3N_4: Enhanced photocatalytic H_2-evolution activity and mechanism insight, Chem. Eng. J. 401 (2020), 126135.